Michael Huxley, Campbell J. Coghlan, Alexandre Burgun, Andrew Tarzia, Kenji Sumida, Christopher J. Sumby, and Christian J. Doonan

Site-specific metal and ligand substitutions in a microporous Mn^{2+}-based metal–organic framework

Dalton Transactions, 2016; 45(10):4431-4438

Published at: http://dx.doi.org/10.1039/C5DT05023E

Dalton Transactions

ARTICLE

Site-Specific Metal and Ligand Substitutions in a Microporous Mn^{2+}-Based Metal-Organic Framework

Received 00th January 20xx,
Accepted 00th January 20xx

DOI: 10.1039/x0xx00000x

www.rsc.org/

Michael Huxley, Campbell J. Coghlan, Alexandre Burgun, Andrew Tarzia, Kenji Sumida,* Christopher J. Sumby,* and Christian J. Doonan*

The precise tuning of the structural and chemical features of microporous metal-organic frameworks (MOFs) is a crucial endeavour for developing materials with properties that are suitable for specific applications. In recent times, techniques for preparing frameworks consisting of mixed-metal or ligand compositions have emerged. However, controlled spatial organisation of the components within these structures at the molecular scale is a difficult challenge, particularly when species possessing similar geometries or chemical properties are used. Here, we describe the synthesis of mixed-metal and ligand variants possessing the Mn_3L_3 (Mn-MOF-1; H_2L = bis(4-(4'-carboxyphenyl)-3,5-dimethylpyrazolyl)methane) structure type. In the case of mixed-ligand synthesis using a mixture of L and its trifluoromethyl-functionalised derivative (H_2L' = bis(4-(4'-carboxyphenyl)-3,5-di(trifluoromethyl)pyrazolyl)methane), a mixed-ligand product in which the L' species predominanantly occupies the pillar sites lining the pores is obtained. Meanwhile, post-synthetic metal exchange of the parent Mn_3L_3 compound using Fe^{2+} or Fe^{3+} ions results in a degree of cation exchange at the carboxylate clusters and metalation at the pillar bispyrazolate sites. The results demonstrate the versatility of the Mn_3L_3 structure type toward both metal and ligand substitutions, and the potential utility of site-specific functionalisations in achieving even greater precision in the tuning of MOFs.

Introduction

Metal-organic frameworks (MOFs)[1] are an emerging class of porous materials that have received intensive investigation in recent years due to their high surface areas, and structural and chemical tunability. These features are attractive for a wide range of applications, including gas storage, molecular separations, heterogeneous catalysis, and their integration within functional devices.[2] While the large library of MOFs now available to researchers encompass a broad range of properties, there is an increasing need for the development of techniques that facilitate molecular-level manipulations of their framework compositions to engender an even greater degree of control over the properties of the materials.

In the area of mixed-metal and mixed-ligand MOFs, a number of preparative strategies have emerged that afford functionalised variants of existing structure types, and considerable effort has also been directed toward the discovery of unique structure types that depend on the mixed compositions for their assembly. These synthetic methods can generally be classified into direct synthetic methods that employ mixed-component reaction solutions,[3] and post-synthetic modification that induce exchange or insertion at the metal nodes[4,5] (single ions or clusters) or organic linkers constituting the framework.[6] These methods generally lead to statistical mixtures (i.e. solid solutions) of the components throughout the crystals, and in this context, examples of structure types that allow site-specific manipulations have remained rare. Furthermore, expansion of the synthetic scope of such mixed-metal and ligand systems is expected to provide greater insight related to the influence of such modifications on the framework properties.

With this in mind, we selected the microporous Mn_3L_3 (Mn-MOF-1; H_2L = bis(4-(4'-carboxyphenyl)-3,5-dimethylpyrazolyl)methane) compound for investigation as a potentially versatile platform for systematic metal and ligand substitutions.[7] This material features free bispyrazolate coordination sites that are available for post-synthetic metal insertions, providing the opportunity for the composition of the metal component to be tuned at both the metal node and at the bispyrazolate sites. Moreover, the incorporation of linkers with additional functionalisation at the periphery of the bispyrazolate moieties is also of interest for tuning the metal binding affinity, as well as the dynamic properties of the framework. Herein, we describe the synthesis and characterisation of a series of frameworks in which a trifluoromethyl-functionalised derivative of L (H_2L' = bis(4-(4'-carboxyphenyl)-3,5-di(trifluoromethyl)pyrazolyl)methane) is introduced into the framework. Interestingly, the L' linker is demonstrated to principally occupy just one of the two unique

Centre for Advanced Nanomaterials, School of Physical Sciences, University of Adelaide, SA 5005, Australia. Email: kenji.sumida@adelaide.edu.au; christopher.sumby@adelaide.edu.au; christian.doonan@adelaide.edu.au.

†Electronic Supplementary Information (ESI) available: Full experimental procedures, powder X-ray diffraction data, thermogravimetric analysis data, adsorption isotherms, and additional discussion. See DOI: 10.1039/x0xx00000x

linker positions within the framework, despite the use of a one-pot, mixed-ligand synthetic procedure. Further, the outcomes of post-synthetic metal exchange reactions on the parent Mn_3L_3 compound with Fe^{2+} and Fe^{3+} cations are probed, which are demonstrated to afford mixed-metal compositions while preserving the original framework connectivity. The results serve to demonstrate the versatility of the Mn_3L_3 structure type toward both metal and ligand substitutions, and the potential utility of site-specific functionalisation in preparing MOFs with precisely tuned properties.

Experimental Section

Unless otherwise stated, all preparations of the organic compounds were performed under an Ar atmosphere using standard Schlenk techniques with dried and degassed solvents. All MOF synthesis reactions were carried out in the air. All reagents except 4-bromo-bis(3,5-trifluoromethyl)pyrazole[8] were obtained from commercial vendors and used without further purification. Powder X-ray diffraction data were collected on a Bruker Advance D8 diffractometer equipped with a capillary stage using Cu Kα radiation (λ = 1.5418 Å). NMR spectra were recorded on a Varian 500 MHz spectrometer operating at 23 °C and equipped with a 5 mm probe. Thermogravimetric analysis was performed on a Perkin-Elmer STA-6000 instrument using a nitrogen flow. Adsorption isotherms were collected on a Micromeritics ASAP 2020 instrument using liquid nitrogen (77 K), dry ice/acetone (195 K) and water (298 K) baths for the N_2, CO_2, and H_2O isotherms, respectively. Single-crystal X-ray diffraction data were collected on the MX1 beamline of the Australia Synchrotron (λ = 0.71073 Å) – see the Supporting Information for full experimental details.

Synthetic Procedures

Bis(4-bromo-3,5-di(trifluoromethyl)pyrazolyl)methane (1). A previously reported method for the synthesis of bis(3,5-di(trifluoromethyl)pyrazolyl)methane was adapted.[9] A solution of 4-bromo-3,5-trifluoromethylpyrazole (1.5 g, 5.3 mmol) in anhydrous DMF (3.2 mL) was added dropwise to a vigorously stirred mixture of NaH (0.18 g of a 60% paraffin oil dispersion) in anhydrous DMF (1.6 mL). Diiodomethane (0.32 mL, 3.9 mmol) was then added, and the mixture was heated at 80 ˚C for 2 days. The mixture was cooled to room temperature, poured into diethyl ether (50 mL), and the organic layer was washed with aqueous K_2CO_3 solution (3 × 20 mL), brine (1 × 20 mL), dried over $MgSO_4$. The solvent was evaporated under a reduced pressure, and the resulting brown oil was cooled in a salted ice-bath to yield crude **1** as a brown solid (1.7 g). This was kept under vacuum for 2 days to remove a diiodomethane impurity to afford the pure product as an off-white solid (1.2 g, 75%). ^{1}H NMR (500MHz, $CDCl_3$): δ(ppm) 6.60 (s, CH_2); ^{19}F NMR (500MHz, $CDCl_3$): δ(ppm) -57.72 (s, CF_3), δ(ppm) -63.18 (s, CF_3).

Bis(4-(4'-ethoxyphenyl)-3,5-di(trifluoromethyl)-pyrazolyl) methane (2). To a mixture of **1** (540 mg, 0.9 mmol), 4-phenylboronic acid ethyl ester (800 mg, 4.1 mmol) and K_2CO_3 (2.48g, 17.9 mmol) in dioxane (30 mL) was added $Pd(PPh_3)_4$ (170 mg, 0.15 mmol). After degassing the mixture for 20 min, the mixture was heated at 90 ˚C for 5 days. After cooling to room temperature, the solvent was evaporated to yield a dark brown solid which was dissolved in chloroform. The solution was filtered, and removal of the solvent resulted in crude **2** as a dark brown solid. The pure product was obtained following purification *via* column chromatography (silica gel, dichloromethane) as a white solid (280 mg, 44%). ^{1}H NMR ($CDCl_3$): δ(ppm) 1.43 (t, CH_3, J=7.2 Hz), 4.43 (q, CH_2, J= 7.1 Hz), 6.74 (s, CH_2), 7.42 (d, 2H, Ar-H, J= 8.3Hz), 8.13 (d, 2H, Ar-H, J= 8.6 Hz); ^{19}F NMR (500 MHz, $CDCl_3$): δ(ppm) -55.85 (s, CF_3), -60.46 (s, CF_3).

Bis(4-(4'-carboxyphenyl)-3,5-di(trifluoromethyl)pyrazolyl)methane (H_2L'). **2** (180 mg, 0.25 mmol) and aqueous KOH (1.8 mL, 2 M) were combined in methanol (7.2 mL), and the resulting mixture was heated at reflux for 20 h. After cooling to room temperature, the solution was filtered and acidified to pH 1 with concentrated HCl. The resulting precipitate was collected under filtration and washed with water to yield H_2L' as a white solid (160 mg, 96 %). IR ν_{max}(neat, cm^{-1}): 2996 (w, O-H), 2892 (w, O-H), 2674 (w, O-H), 2547 (w, O-H), 1698 (C=O); 1421 (C=C); 1284 (s), 1238 (C-F), 1181 (C-F), 1169 (C-F), 1127 (C-F); ^{1}H NMR ($(CD_3)_2SO$): δ(ppm) 7.04 (s, CH_2), 7.49ppm (d, Ar-H, J= 8.1 Hz), 8.04 (d, Ar-H, J= 8.3 Hz), 13.21 (br, OH); ^{19}F NMR ($(CD_3)_2SO$): δ(ppm) -59.28 (s, CF_3), -55.46 (s, CF_3); ^{13}C NMR ($(CD_3)_2SO$) δ(ppm) 167.17, 132.13, 131.59, 130.40, 129.73, 127.59, 123.56, 109.7, 66.16, 65.60.

Mixed-ligand frameworks. In a typical synthesis, the ligands L and L' (total quantity: 0.025 mmol) and $MnCl_2{\cdot}4H_2O$ (8.1mg, 0.040 mmol) were combined in a glass vial. DMF (2.0 mL) and H_2O (1.0 mL) were then added, and the resulting mixture was sonicated for 15 min. The vial was sealed and heated under static conditions at 100 ˚C in a pre-heated oven for 5 days to yield colorless, block shaped crystals. The solid was isolated and washed with DMF (3 × 20 mL) and methanol (3 × 20 mL), and activation for adsorption experiments was performed by heating at 100 ˚C *in vacuo* for a period of 24 h. The composition of the solid was deduced by digesting the solid in DCl in $(CD_3)SO$, followed by ^{1}H and ^{19}F NMR spectroscopy.

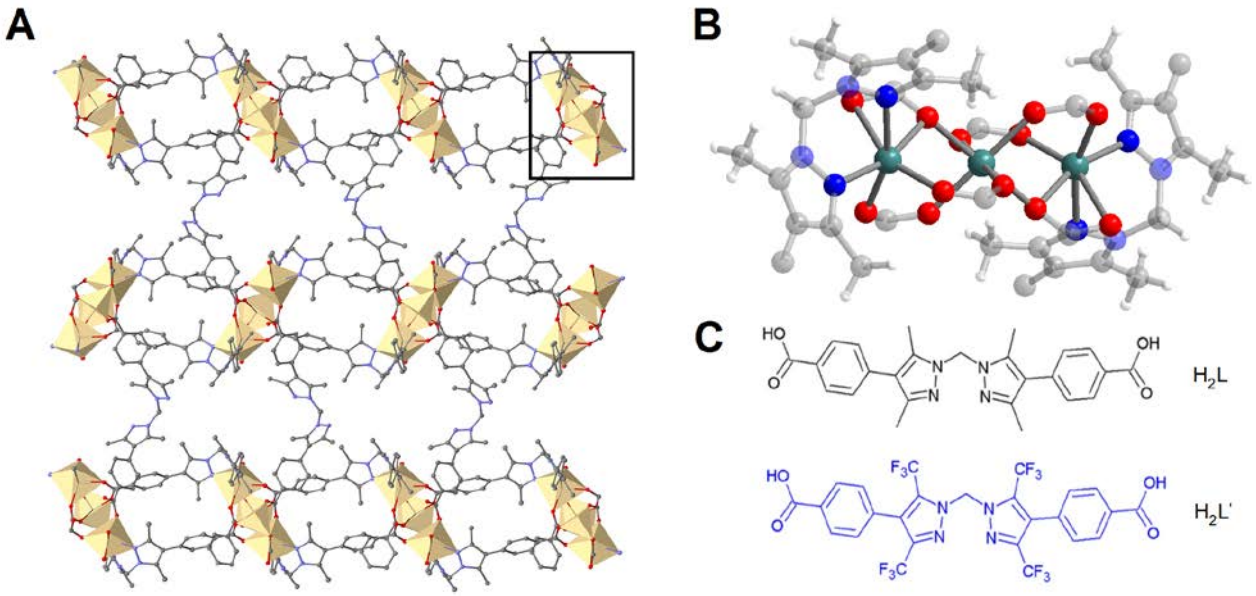

Fig. 1. (A) A portion of the crystal structure of M_3L_3,[7] as observed along the crystallographic *c*-direction. The structure features square grids in the *bc*-plane that are bound by axial pillar linkers having bispyrazolate moieties available for metal binding; (B) A view of the trinuclear Mn_3^{6+} cluster enclosed by the black box; and (C) molecular structures of the bis(4-(4'-carboxyphenyl)-3,5-dimethylpyrazolyl)methane (H_2L) and bis(4-(4'-carboxyphenyl)-3,5-di(trifluoromethyl)methane (H_2L') employed in this work. Teal, grey, blue, red, and white spheres represent Mn, C, N, O, and H atoms, respectively. H atoms are omitted from panel (A) for clarity.

Mixed-metal frameworks. In a typical procedure (described for $Fe(acac)_3$ as the iron source), the as-synthesised material, Mn_3L_3 (24.0 mg), was firstly solvent-exchanged with dry acetonitrile. The solvent was decanted and replenished five times, each time allowing the crystals to soak for 10 min between each cycle. Then, $Fe(acac)_3$ (30.0 mg; $acac^-$ = acetylacetonate) was added to the vial and the resulting mixture was placed in an oven pre-set at 65 °C for 1, 5 or 10 days. The orange suspension was then allowed to cool to room temperature, and the solvent was exchanged with freshly dried acetonitrile (× 5). The solvent was decanted and the crystals were dried under a dynamic vacuum to afford the Fe-exchanged material. The same exchange procedure was performed for $FeCl_2{\cdot}4H_2O$ and $FeCl_3$, using ethanol and acetonitrile as the exchange solvents, respectively. X-ray diffraction data for these compounds were collected at 100(2) K on the MX-1 beamline of the Australian Synchrotron (λ = 0.71073 Å). CCDC accession codes 1143923 and 1143924 contain the structural data associated with the samples exchanged with $FeCl_3$ and $FeCl_2{\cdot}4H_2O$, respectively. Further details associated with the data collection and structural refinement are provided in the supporting information (see also Table S1).

Inductively-coupled plasma mass spectrometry (ICP-MS). Each sample was synthesized separately three times and the bulk dissolved in a 2% HNO_3 sample at 65 °C overnight. The samples where then filtered through a 45 µm filter to remove any ligand and particulate matter. Each sample was then diluted to within the measurement range. The samples where then analysed on an Agilent 7500cs solution ICP-MS instrument to evaluate the Fe-to-Mn ratio, and the average of the three samples were tabulated in Table 1 (see below).

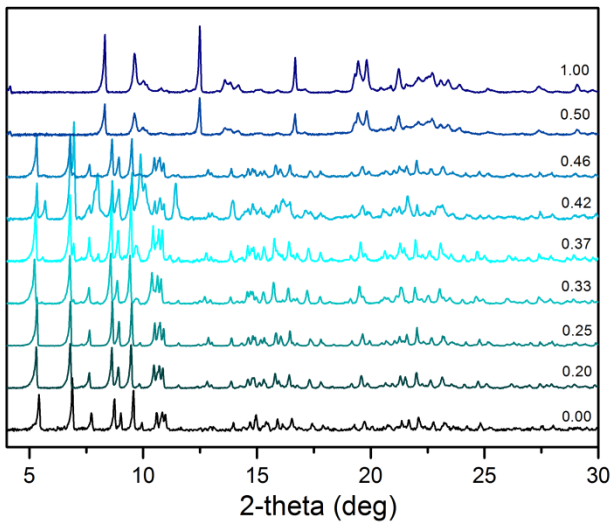

Fig. 2. Powder X-ray diffraction patterns collected for materials synthesised with varying ratios of the ligands L and L'. The fraction associated with each plot represents the mole ratio of L' in the mixture, which is varied from 0.00 (resulting in pure Mn_3L_3) to 1.00.

Results and Discussion

Prior to discussing the preparation and characterisation of the new materials, we first briefly review the structural details of the parent Mn_3L_3 structure type[7] that are relevant to the manipulations in the mixed-component systems.

Mn_3L_3 structure type

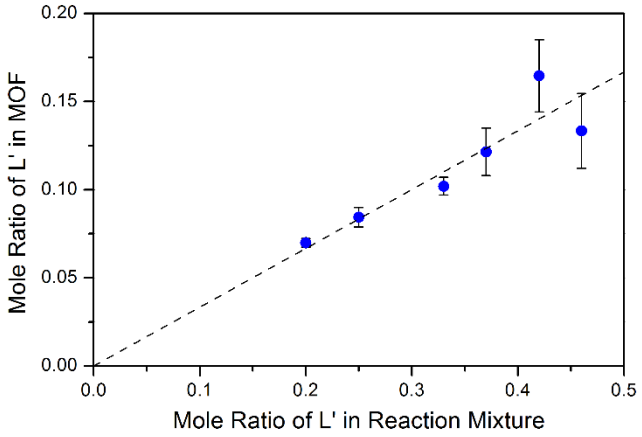

Fig. 3. A plot of the proportion of the trifluoromethyl-substituted linker (L') within the MOF as calculated from the NMR data as a function of the quantity of L' in the reaction mixture. The dotted line represents the line of best fit to the data, while the error bars represent one standard deviation.

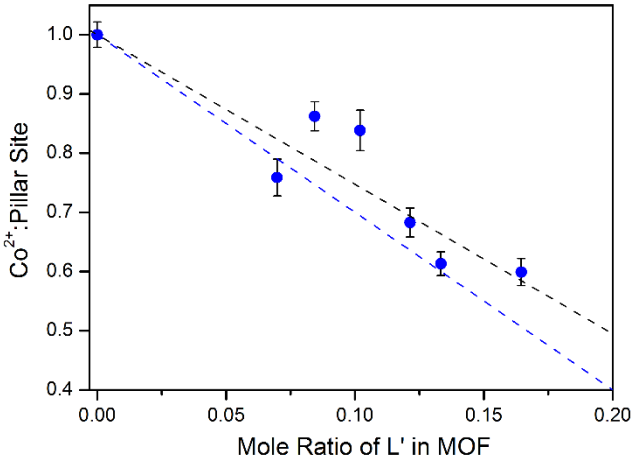

Fig. 4. A plot of Co^{2+} uptake per pillar site in the MOF from ICP-MS data as a function of the quantity of trifluoromethyl-substituted linker (L') within the MOF. The black dotted line represents the line of best fit to the data, while the error bars represent one standard deviation. The blue dotted line represents the expected overall population of Co^{2+} ions per pillar site assuming all of the L' linker within the MOF occupies the pillar site, and does not participate in Co^{2+} binding.

The structure of Mn_3L_3 is presented in Fig. 1A. This material consists of linear Mn_3^{6+} clusters (see Fig. 1B), wherein adjacent Mn^{2+} centres are bridged by a total of three carboxylate groups of three different ligand molecules: two that are bound in a bridging mode through both oxygen atoms, and one bridging through just one of the oxygen atoms. The central Mn^{2+} centre is in an octahedral ligand environment bound solely by the carboxylate groups, while the terminal centres are bound by four carboxylate oxygen atoms and are further capped by a chelating bispyrazolate moiety to complete the distorted octahedral coordination environment. Two-thirds of the linker molecules in the structure bridge adjacent Mn_3^{6+} clusters in the crystallographic *ac*-plane to form a square grid. The remaining one-third of ligand molecules axially pillar the individual grids to form a microporous three-dimensional network (space group: *C*2/*c*) with a moderate BET surface area of 700 m^2/g. Note that in the activated form of the Mn_3L_3 framework, the bispyrazolate groups in the pillar ligands are free of coordinated metal ions, and this has previously been the focus of post-synthetic insertion reactions using a range of metal ions, including Co^{2+} and Rh^{+}.[7]

Mixed-ligand frameworks

The synthesis of mixed-ligand frameworks was carried out by systematically tuning the composition of the reaction mixture, while holding constant all other reaction conditions employed in the synthesis of the Mn_3L_3 compound. Specifically, the mole ratio of the trifluoromethyl-substituted linker L′ was varied with respect to the parent ligand L (see Fig. 1C) between 0.00 (all L) to 1.00 (all L'). Crystalline materials were obtained for all reactions, and the powder X-ray diffraction patterns collected for selected samples are shown in Fig. 2. The data revealed that the parent Mn_3L_3 structure type was preserved up to a mole ratio of 0.46. Within this range, a gradual shift in the peaks to lower 2θ angles was observed an increasing content of L', potentially reflecting a slight expansion in the unit cell parameters due to the bulkier trifluoromethyl substituents present within the L' linker. Interestingly, at 0.50 and higher L' compositions, a new crystalline phase was obtained in high purity up to an L' content of 1.00. Further, observation of the crystal morphology showed that the crystals adopt a rhombus-shaped morphology for the parent Mn_3L_3 phase (Fig. S1), while at a mole ratio up to 0.46, a uniform, block-shaped morphology was observed (Fig. S2). At higher proportions of L', very thin plates not suitable for single-crystal X-ray analysis were obtained (Fig. S3). These changes in crystal morphology coincide with the L' levels in the reaction mixture that induce changes in the powder X-ray diffraction patterns, providing further evidence for changes in the composition and structure of the resulting frameworks.

The degree of incorporation of L' into the materials was examined via a combination of ^{1}H- and ^{19}F-NMR experiments[10] for samples that displayed powder X-ray diffraction data matching that of the parent Mn_3L_3 structure type. Since the methylene bridge of L and L' display distinct ^{1}H-NMR chemical shifts (δ 6.28 and 7.04 ppm, respectively), the content of L' in the MOF sample was able to be estimated via integration of the respective methylene signals. Interestingly, analysis of the peak integrals revealed a linear relationship between the mole ratio of L' in the framework and the mole ratio within the reaction mixture (see Fig. 3). A maximum ratio of ca. 0.17 was observed for a reaction mixture containing a mole ratio of 0.42 in L'. Note that the samples obtained using reaction mixtures containing higher levels of L' (i.e. 0.5 and higher) did not exhibit any content of the L linker, indicating the formation of a new phase consisting of only L' linkers.[11]

Following elucidation of the composition of the samples, the impact of the mixed composition on the metal uptake (i.e. metal insertion at the pillar bispyrazolate binding site) was investigated. Here, each sample was immersed in a methanol solution containing an excess of $CoCl_2{\cdot}4H_2O$, and heated at 65 °C for a period of 16 h. After this time, the products were subjected to energy dispersive X-ray (EDX) and inductively-coupled plasma mass spectrometry (ICP-MS) experiments.

Interestingly, the Co^{2+} content linearly decreased with an increasing composition of the L' linker (black dotted line in Fig. 4). Previous crystallographic investigation of the parent Mn_3L_3 compound metalated with Co^{2+} cations revealed full occupancy of the bispyrazolate binding sites under the same reaction conditions.[7] Therefore, we surmised that the decrease in Co^{2+} uptake is a result of the L' linker being unable to accommodate metal species at its bispyrazolate moiety under these conditions. Further, the slope of the linear fit in Fig. 5 was a close match with the maximum decrease in Co^{2+} metalation that would be observed for a case where all of the L' occupied the pillar site (blue dotted line in Fig. 4), suggesting that site-specific substitutions were obtained with chiefly the L linkers occupying the square grid positions in the framework.

In order to elucidate the origin of this observation, we firstly investigated the binding environment around the Mn_3^{6+} cluster of the metal node in more detail. The similarity in powder X-ray diffraction patterns between the parent Mn_3L_3 material and the mixed-ligand frameworks suggested that the ligand environments about the Mn^{2+} ions were structurally similar. Modeling of the substitution of the position of the methyl groups on the 3 and 5 positions of the pyrazolate rings with trifluoromethyl groups (Fig. S4) resulted in larger van der Waals radii of the substituent groups, which were incompatible with the packing of the ligand groups around the cluster. This further supports the L' linker being directed to the pillar sites of the structure, where only their carboxylate groups, which are unaffected by the functionalisation on at pyrazolate rings, participate in binding to the metal clusters.

Further, DFT calculations were carried out on a truncated portion of the linker in order probe the absence of Co^{2+} metalation at the bispyrazolate site of the L' linkers when in the pillar position. Firstly, we note that in the Mn_3L_3 compound, the metalation results in a structural change at the pillar linkers necessitating a rotation about the methylene hinge within the L linker (see Fig. S5, upper panel). We suspected that this rotation was greatly hindered in the L' linker due to the greater steric bulk of the trifluoromethyl groups.[12] Computation of the molecular energy as a function of the dihedral angle between the two pyrazolate rings showed a considerably larger barrier to rotation in L' compared to L (see Fig. S5, lower panel), which is expected to inhibit access to the conformation necessary to bind metal ions. In addition to this steric factor, the binding of Co^{2+} is also likely to be significantly weaker within L' due to the decreased donor strength of the bispyrazolate groups due to the electron-withdrawing nature of the trifluoromethyl substituents. Thus, from these modelling data, it can be deduced that the L' component favourably occupies the pillar position in the crystal structure, and the trifluoromethyl-substituted bispyrazolate groups are unable to act as binding sites for metal ions, resulting in a lower Co^{2+} uptake as the concentration of L' within the structure is increased.

After elucidation of the composition and structure of the mixed-ligand systems, the material containing the maximum quantity of L' linkers (reaction L' content: 0.42; composition: $Mn_3L_{2.49}L'_{0.51}$) was subjected to gas sorption experiments. The N_2 adsorption isotherm collected at 77 K presented in Fig. S6 represents a type-I isotherm reflecting the microporous nature of the structure, while the slightly decreased total adsorption capacity reflects the increased steric bulk and mass of the trifluoromethyl groups compared to the methyl groups in the parent compound. Furthermore, as shown in Fig. S7, the material exhibits a stepped CO_2 adsorption isotherm at 195 K, which is consistent with the dynamic nature of the parent Mn_3L_3 framework. However, the position of the step is located at significantly higher pressures once the L' linker is introduced, presumably due to its larger barrier to rotation about the methylene hinges as described above. Similar observations are observed for the adsorption isotherm for H_2O (293 K; Fig. S8).

Table 1. Metal composition as obtained by ICP-MS for Mn_3L_3 samples after treatment with Fe-containing solutions

Metal source	T (°C)	t (days)	Mn	Fe	±*
$FeCl_2·4H_2O$	25	1	77.5	22.5	3.1
		5	63.6	36.4	0.3
	60	1	71.6	28.4	1.3
		5	71.5	28.5	3.2
$FeCl_3$	25	1	75.2	24.8	1.5
		5	77.5	22.5	0.9
	60	1	42.4	57.6	13.0
		5	1.4	98.6	0.6
$Fe(acac)_3$	25	1	98.9	1.1	0.4
		5	96.2	3.8	2.9
	60	1	97.1	2.9	1.5
		5	94.9	5.1	0.9

*indicates standard deviation

Mixed-metal frameworks

The ability of the Mn_3L_3 compound to accommodate functionalised linkers prompted the investigation of post-synthetic metal exchange and metalation reactions. Owing to its redox activity and its potential for use in catalytic reactions, several Fe^{2+}- and Fe^{3+}-containing metal sources, namely $FeCl_2·4H_2O$, $Fe(acac)_3$, and $FeCl_3$ were selected for testing. Here, samples of Mn_3L_3 were suspended in a concentrated solution of the metal salt in an organic solvent at room temperature or under mild heating (60 °C), and the composition of the material was analyzed by ICP-MS after 1 and 5 days (see Table 1). As can be clearly observed by the data, the metal source, soaking time, and reaction temperature each significantly influenced the composition of the resulting product.

Metal source. Here, minimal exchange was observed with $Fe(acac)_3$ compared to the chloride salts, potentially due to the relative stability of the complexes in solution, and the bulky nature of the ligands inhibiting the complex from freely diffusing within the pores. The highest exchange is observed with $FeCl_3$, which are expected to diffuse more rapidly due to its smaller molecular size and relatively strong binding within the binding environments found in the metal clusters and at the chelating bispyrazolate moieties.

Reaction time. Higher iron loadings were observed at longer reaction times, particularly for those maintained at room temperature. This can be ascribed to the diffusion of the iron source and the rate of exchange and metalation requiring a longer time to reach an equilibrium at lower temperatures.

Soaking temperature. In addition to the rate of loading, the extent of exchange and metalation was higher at higher temperatures. Interestingly, heating of the $FeCl_3$ reaction mixture at 60 °C over 5 days resulted in near complete exchange of the metal cations.

Single crystal X-ray structure determinations

Following the characterisation of the chemical composition of each of the iron-exchanged samples, single-crystals of the material following a 5-day exchange reaction at 60°C using $FeCl_2{\cdot}4H_2O$ (iron content: 28.5 ± 3.2%) and $FeCl_3$ (iron content: 98.6± 0.6%) were subjected to X-ray diffraction experiments (see Supporting Information and Table S1 for further experimental details). These crystalline samples are homogenous in appearance and the crystals were light and dark orange in colour (see Fig. S9-10), consistent with moderate and high levels of Fe incorporation, respectively. The crystallographic analysis is complicated by competing processes occurring during these metalations, the exchange of metals at the nodes of the MOF, metalation of the well-established metal binding site and possibly a minor contribution from residual metal salts in the pores. Despite this, these structures confirmed the original framework connectivity and provide some further insight into the process of metalation, specifically excluding significant pore loading of Fe^{3+} for $Fe_3L_3{\cdot}FeCl_3$.

Structure of $Fe_3L_3{\cdot}FeCl_3$. For the $FeCl_3$ exchanged sample, the iron content was established as 98.6± 0.6% indicating that, within the crystals, Fe not only occupies the free coordinating site of Mn_3L_3 but also substitutes for the Mn^{2+} centres of the node. Analysis of the diffraction data was consistent with quantitative exchange of the metals at the metal nodes, as well as a full occupancy at the bispyrazolate binding sites. Importantly, no evidence for significant pore-bound Fe species was observed in the single crystal structure.[13] The lack of Mn in the samples led us to model the data with a trinuclear Fe_3 node in the MOF. A detailed examination of the metal-ligand bond distances within the trinuclear clusters revealed only minor differences with those of the parent Mn_3L_3 compound, providing support for the presence of Fe^{2+} as opposed to the reactant Fe^{3+} within the clusters. While the precise mechanism for the reduction of Fe^{3+} to Fe^{2+} upon metal exchange has not yet been established, trinuclear Mn-based clusters have been known to participate in redox chemistry, potentially acting as a sufficiently strong reductant under these conditions to reduce Fe^{3+} ions with a concomitant liberation of a Mn^{3+} ion.[14] Based upon the inductively-coupled plasma mass spectrometry (ICP-MS) data, a very small residual amount of Mn is still present in these crystals but, given the low levels, we did not include this in the model for structure refinement.

While this structure importantly confirms there is no significant electron density in the pores of the MOF, we also examined the ligand-based metalation site within the material. On the basis of the ICP-MS and structural data, metalation at the bis-pyrazole site proceeds in high yield but the form of the metalated product is unclear. In our previous work,[7,13] the identity of the post-synthetic metalation product could be readily discerned from difference electron density maps. To shed light on the structure of the product here, we examined the F_{obs} electron density maps which indicate appreciable disorder of the added metal complex. The metal site is ill-defined, consistent with there being a second complex with a different geometry and/or oxidation state disordered over the site. Specifically, the site has two significant regions of electron density above and below the plane formed by the pyrazole nitrogen atoms and the Fe centre (see Fig. S11). We have modelled the data as an octahedral Fe^{3+} cation (due to slightly shorter Fe-N bonds of 2.084(8) Å) possessing two inner-sphere chloride ions and a third outer-sphere anion within the pores of the framework (see panel d of Fig. S11), but the disorder present limits ultimate identification and model refinement. Interestingly, this arrangement of the chloride ions is similar to that observed within iron salts such as $FeCl_3{\cdot}6H_2O$, which contains two apical chlorides and four equatorial water molecules, and an outer-sphere chloride ion for charge balance.

Structure of $Mn_{3-x}Fe_xL_3{\cdot}0.4FeCl_2$ (x = 0.55). In the case of the $FeCl_2$-exchanged sample, partial occupancy of *ca* 0.2 (40% metalation due to the mirror plane) is observed at the bispyrazolate moiety, which was established by trial refinement. This observation coupled with the 28.5 ± 3.2% Fe occupancy in the MOF as determined by ICP-MS leads us to suggest that *ca* 0.5-0.6 equivalents of Fe occupy the trinuclear node of the MOF. While there is potential for a minor amount of Fe loading into the pores to remain after the washing cycles, the lack of significant electron density in the pores further supports this rationalisation and the assigned formula $Mn_{3-x}Fe_xL_3$ (x = 0.55). Given the similarities between Fe^{2+} and Mn^{2+} cations, the bond lengths and angles around the metal node are relatively unchanged.

The low occupancy Fe centre bound to the bis-pyrazole coordinating site is surprisingly well-ordered, and the octahedral coordination environment (FeN_2O_3Cl) supports retention of the Fe^{2+} oxidation state based on the longer Fe-N distance of 2.218(9) Å. Given the relatively low occupancy nature of this site and a limited amount of evidence for the anion species in the pores, we have limited the discussion to this observation. The pores of the MOF contain a peak, assigned as a chloride (0.2 occupancy, 40%), to provide charge balance to the octahedral Fe centre, that sits in the pocket typically occupied by anions within the MOF structure.[7,13] There is additional electron density in this site (largest peak = 2.958 e·Å^3, unmodeled before application of the SQUEEZE routine of Platon[15]), which is potentially ascribable to a partial occupancy of solvent molecules occupying this position in the absence of an anion. Note that the ability of these bispyrazolate moieties to accommodate both $Fe^{2+}$and Fe^{3+} ions is of interest in catalytic processes involving redox

transformations, and studies directed toward understanding the reactivity of these sites is currently underway.

Summary and Outlook

The foregoing work has described experiments for preparing frameworks of the Mn_3L_3 structure type with compositions having a mixture of organic linkers or metal cations. As discussed, in the case of the use of the trifluoromethyl-substituted L' linker, the substitutions occur solely at the pillar linker site, and metalation does not occur at the bispyrazolate moiety owing to the hindered rotation about its methylene bridge, as well as the weaker binding stemming from the electron-withdrawing nature of the substituents. Although such a dilution of available metalation sites will limit the ability to structurally characterize the coordination sphere of the added metal centres, it may actually offer significant benefit in cases where factors such catalyst loading, diffusion rates and heat dissipation require tuning in order to maximise the performance of the support. In the case of metal exchange and insertion, the metal source is demonstrated to have the most significant influence on the magnitude and rate of the conversion. Activating these metalated species to afford exposed metal cations, and understanding the reactivity of these metal sites will be a central focus of future studies with an object of developing enhanced MOF-based catalysts.

Acknowledgements

This research is supported by the Science and Industry Endowment Fund (SIEF). CJD and CJS acknowledge the Australian Research Council (ARC) Future Fellowship scheme for funding under award numbers FT100100400 and FT0991910, respectively. We thank the MX-1 beamline at the Australian Synchrotron for instrument time and technical support. We also acknowledge the NCI National Facility (Canberra, Australia) supported by the Australian Commonwealth Government for computational time used for the DFT studies. We thank Lynton for helpful discussions.

Notes and references

1 (a) O. M. Yaghi, M. O'Keeffe, N. W. Ockwing, H. K. Chae, M. Eddaoudi and J. Kim, *Nature*, 2003, **423**, 705; (b) S. Kitagawa, R. Kitaura and S. Noro, *Angew. Chem., Int. Ed.*, 2004, **43**, 2334; (c) G. Férey, *Chem. Soc. Rev.*, 2008, *37*, 191.

2 For recent reviews covering the emerging applications of metal-organic frameworks, refer to the special themed issues in *Chem. Rev.*, and more recently *Chem. Soc. Rev.*: (a) H.-C. Zhou, J. R. Long and O. M. Yaghi, *Chem. Rev.* 2012, **112**, 673; (b) H.-C. Zhou and S. Kitagawa, *Chem. Soc. Rev.* 2014, **43**, 5415, and references therein.

3 (a) K. Koh, A. G. Wong-Foy and A. J. Matzger, *Angew. Chem., Int. Ed.*, 2007, **47**, 677; (b) H. Deng, C. J. Doonan, H. Furukawa, R. B. Ferreira, J. Towne, C. B. Knobler, B. Wang and O. Yaghi, *Science*, 2010, **327**, 846; (c) S. Marx, W. Kleist, J. Huang, M. Maciejewski and A. Baiker, *Dalton Trans.*, 2010, **39**, 3795; (d) L. Liu, K. Konstas, M. R. Hill and S. G. Telfer, *J. Am. Chem. Soc.*, 2013, **135**, 17731; (e) C. Wang, D. Liu, Z. Xie and W. Lin, *Inorg. Chem.*, 2014, **53**, 1331; (f) A. Sue, R. Mannige, H. Deng, D. Cao, C. Wang, F. Gándara, J. F. Stoddart, S. Whitelam, and O. M. Yaghi, *Proc. Nat. Acad. Sci. U.S.A.*, 2015, **112**, 5591.

4 Examples of metal insertion include: (a) E. D. Bloch, D. Britt, C. J. Doonan, F. J. Uribe-Romo, H. Furukawa, J. R. Long and O. M. Yaghi, *J. Am. Chem. Soc.*, 2010, **132**, 14382; (b) C. Wang, Z. Xie, K. deKrafft and W. Lin, *J. Am. Chem. Soc.*, 2011, **133**, 13445; (c) M. I. Gonzalez, E. D. Bloch, J. A. Mason, S. J. Teat and J. R. Long, *Inorg. Chem.*, 2015, **54**, 2995; (d) T. Toyao, K. Miyahara, M. Fujiwaki, T.-H. Kim, S. Dohshi, Y. Horiuchi and M. Matsuoka, *J. Phys. Chem. C*, 2015, **119**, 8131.

5 Examples of metal ion exchange include: (a) C. K. Brozek and M. Dincă, *Chem. Sci.*, 2012, **3**, 2110; (b) M. Kim, J. F. Cahill, H. Fei, K. A. Prather and S. M. Cohen, *J. Am. Chem. Soc.*, 2012, **134**, 18082; (c) X. Song, T. K. Kim, H. Kim, D. Kim, S. Jeong, H. R. Moon and M. S. Lah, *Chem. Mater.* 2012, **24**, 3065; (d) J.-H. Liao, W.-T. Chen, C.-S. Tsai and C.-C. Wang, *CrystEngComm*, 2013, 3377; (e) C. K. Brozek and M. Dincă, *J. Am. Chem. Soc.*, 2013, **135**, 12886.

6 Examples of organic linker exchange include: (a) B. J. Burnett, P. M. Barron, M. Paul, C. Hu and W. Choe, *J. Am. Chem. Soc.*, 2011, **133**, 9984; (b) M. Kim, J. F. Cahill, Y. Su, K. A. Prather and S. M. Cohen, *Chem. Sci.* 2012, **3**, 126; (c)T. Li, M. T. Kozlowski, E. A. Doud, M. N. Blakely and N. L. Rosi, *J. Am. Chem. Soc.* 2013, **135**, 11688; (d) M. B. Lalonde, J. E. Mondloch, P. Deria, A. A. Sarjeant, S. S. Al-Juaid, O. I. Osman, O. K. Farha and J. T. Hupp, *Inorg. Chem.* 2015, **54**, 7142.

7 W. M. Bloch, A. Burgun, C. J. Coghlan, R. Lee, M. L. Coote, C. J. Doonan and C. J. Sumby, *Nat. Chem.*, 2014, **6**, 906.

8 A. Maspero. G. Giovenzana, D. Monticelli, S. Tagliapietra, G. Palmisano and A. Penoni, *J. Fluorine Chem.*, 2012, **139**, 53.

9 G. Pampaloni, R. Pelso, D. Belletti, C. Graiff and A. Tiripicchio, *Organometallics*, 2007, **26**, 4278.

10 (a) K. K. Tanabe, Z. Wang and S. M. Cohen, *J. Am. Chem. Soc.*, 2008, **130**, 8508; (b) R. K. Deshpande, J. L. Minnaar and S. G. Telfer, *Angew. Chem., Int. Ed.* 2010, **49**, 4598; (c) H. Deng, C. J. Doonan, H. Furukawa, R. B. Ferreira, J. Towne, C. B. Knobler, B. Wang and O. M. Yaghi, *Science*, 2010, **327**, 849.

11 Note that although attempts to obtain crystals suitable for single-crystal X-ray diffraction analysis were unsuccessful, the material is found to be non-porous by adsorption experiments. Thus, full characterisation was performed only on those materials exhibiting the parent Mn_3L_3 structure type.

12 Single-crystal X-ray diffraction experiments performed on the mixed-ligand frameworks exhibited significant disorder, precluding conclusive refinement of the trifluoromethyl groups of the L' linker.

13 W. M. Bloch, A. Burgun, C. J. Doonan and C. J. Sumby, *Chem. Commun.*, 2015, **51**, 5686.

14 F. Birkelbach, T. Weyhermüller, M. Lengen, M. Gerdan, A. X. Trautwein, K. Wieghart and P. Chaudhuri, *J. Chem. Soc., Dalton Trans.*, 1997, 4259.

15 (a) A.L.Spek, *Acta Crystallogr.*, 2009, **D65**, 148; (b) A.L. Spek, *Acta Crystallogr.*, 2009, **C71**, 9.

Supporting Information for:

Site-Specific Metal and Ligand Substitutions in a Microporous Mn^{2+}-Based Metal-Organic Framework

Michael Huxley, Campbell J. Coghlan, Alexandre Burgun, Andrew Tarzia, Kenji Sumida,* Christopher J. Sumby,* and Christian J. Doonan*

Dalton. Trans.

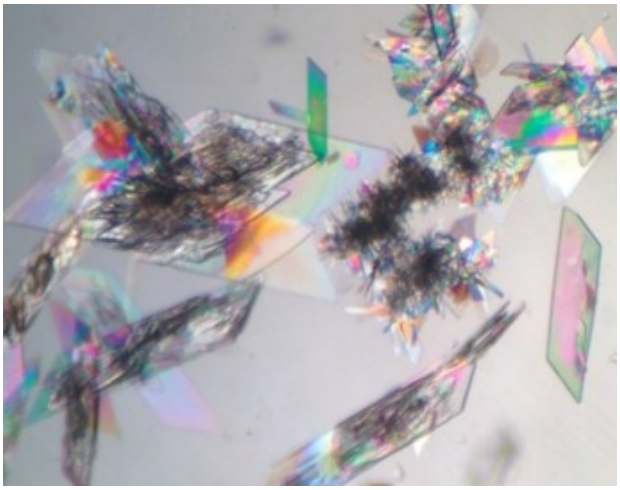

Fig. S1 An optical image showing the as-synthesized form of the parent Mn_3L_3 (L-based) material synthesized using a ratio of L:L' of 1:0.

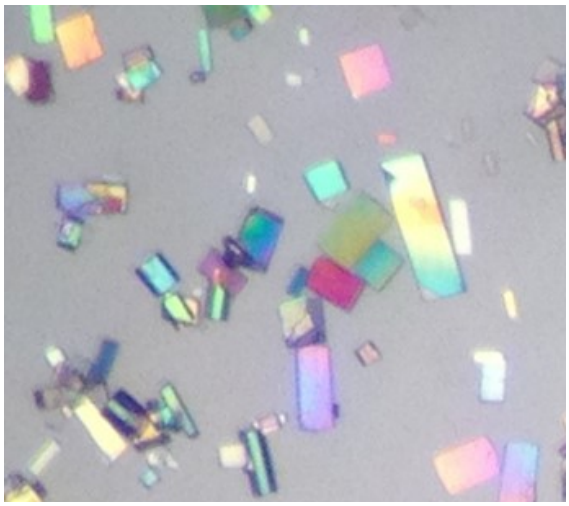

Fig. S2 An optical image showing the as-synthesized form of the mixed-linker material synthesized using a ratio of L:L' of 0.54:0.46.

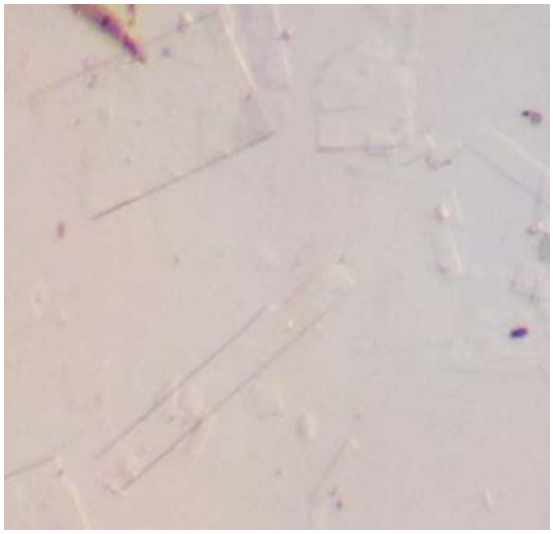

Fig. S3 An optical image showing the as-synthesized form of the L'-based material synthesized using a ratio of L:L' of 0:1.

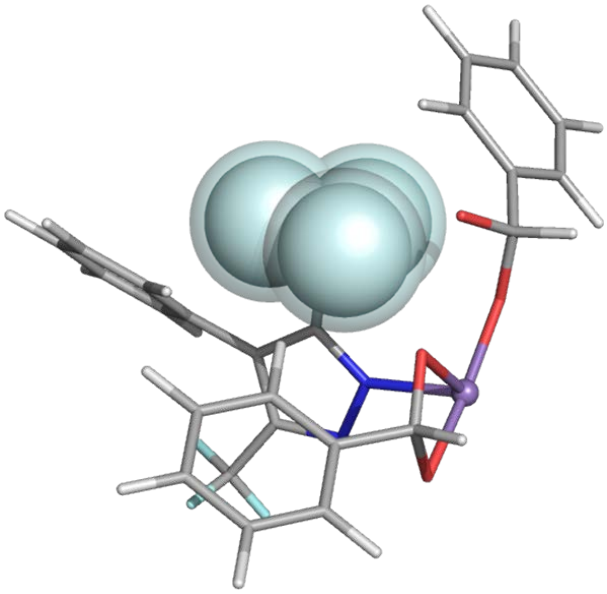

Fig. S4 An enlarged view of the methyl substituent located in the vicinity of the terminal Mn^{2+} ion of the trinuclear Mn_3^{6+} cluster. Upon substitution of the hydrogen atoms (solid spheres; Van der Vaals radius: 120 pm) with fluorine (transparent spheres; 135 pm), an unfavorable steric overlap occurs with the surrounding atoms, leading to the trifluoromethyl-substituted linker being predominantly located at the pillar linker sites. Purple spheres, grey, blue, and red nodes represent Mn, C, N, and O, respectively, while H atoms except on the trifluoromethyl substituent have been omitted for clarity.

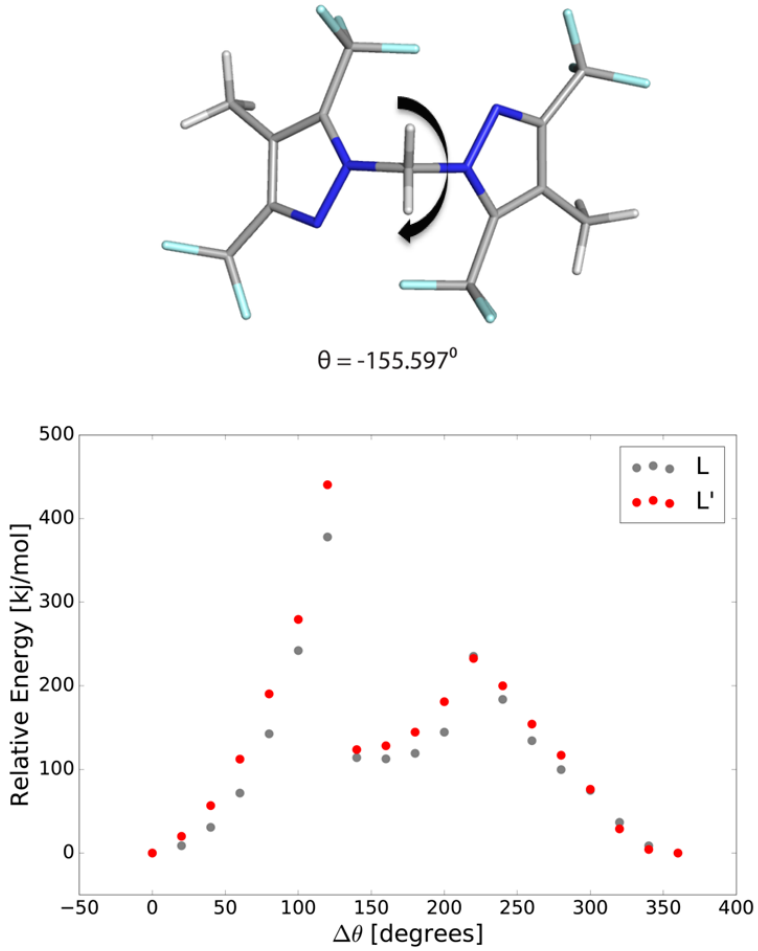

Fig. S5 A view of the truncated trifluoromethyl-substituted bispyrazolate moiety as modelled by density functional theory at the m06/6-311G++ (d,p) level of theory (upper); and relative energies of the molecule at different angles of rotation about the methylene spacer (lower). Here, the energies are computed for a full, 360° rotation of θ (formed by the four nitrogen atoms of the pyrazolate functionalities), calculating the energies every 20°. For the molecular system, the crystallographically-observed angle (θ_0 = -155.6°, $\Delta\theta$ = 0°) in the closed structure is found to be the most favorable conformation, with a local minimum observed for $\Delta\theta$ in the range of 140-160° as observed in the open structure. The rotational barrier is significantly greater in the case of the trifluoromethyl-substituted L' linker, which is consistent with the higher pressures at which the structural reorganization is observed in the adsorption isotherms.

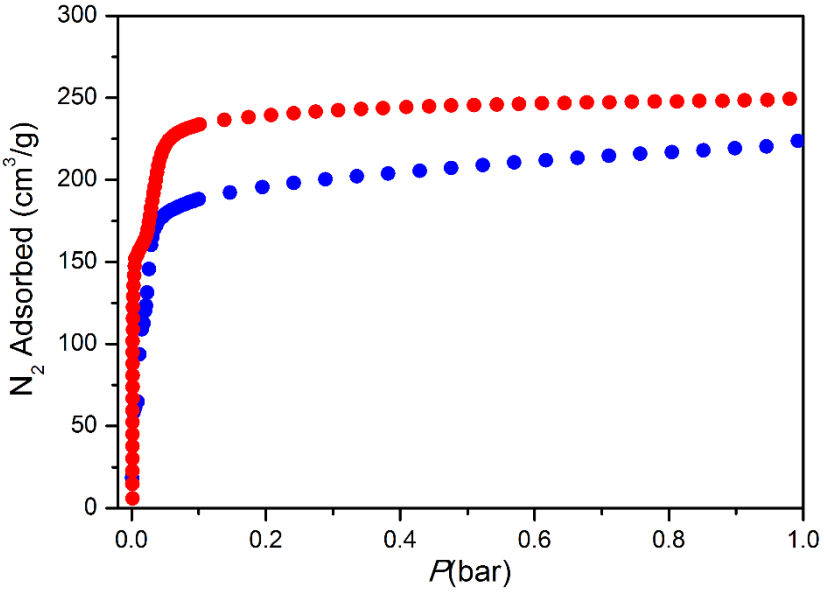

Fig. S6 N_2 adsorption isotherms recorded at 77 K for Mn_3L_3 (red) and $Mn_3L_{2.49}L'_{0.51}$ (blue).

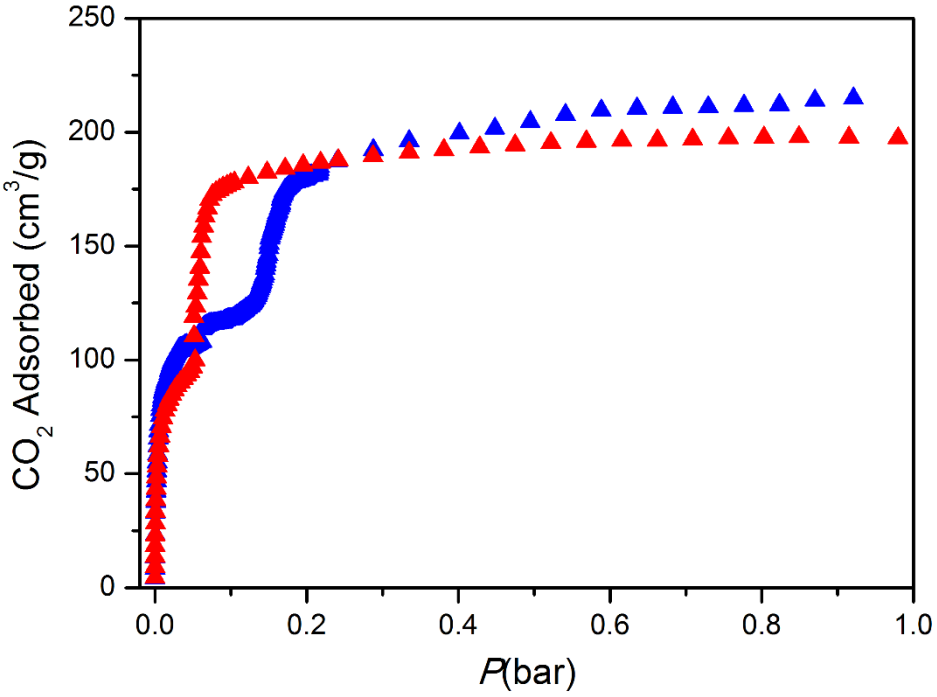

Fig. S7 CO_2 adsorption isotherms recorded at 195 K for Mn_3L_3 (red) and $Mn_3L_{2.49}L'_{0.51}$ (blue).

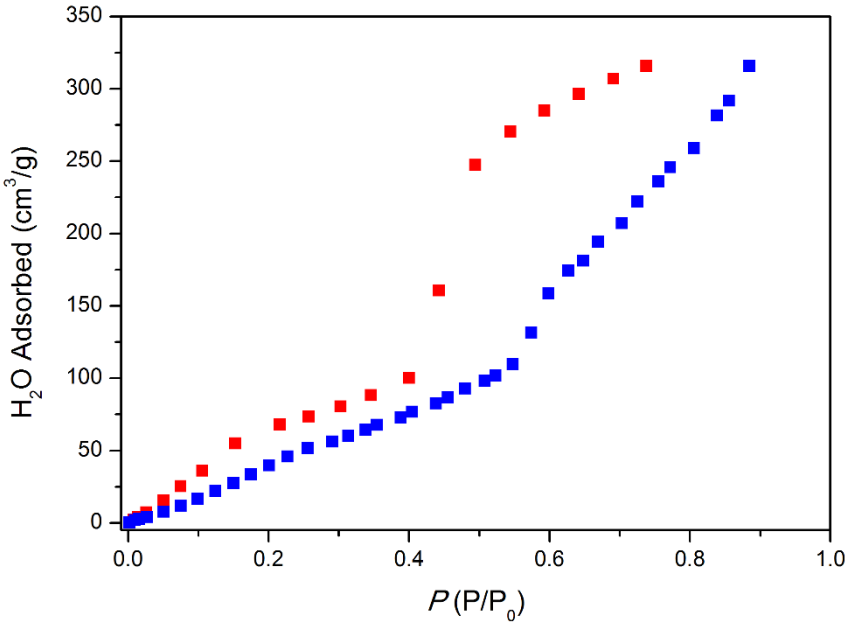

Fig. S8 H_2O adsorption isotherms recorded at 298 K for Mn_3L_3 (red) and $Mn_3L_{2.49}L'_{0.51}$ (blue).

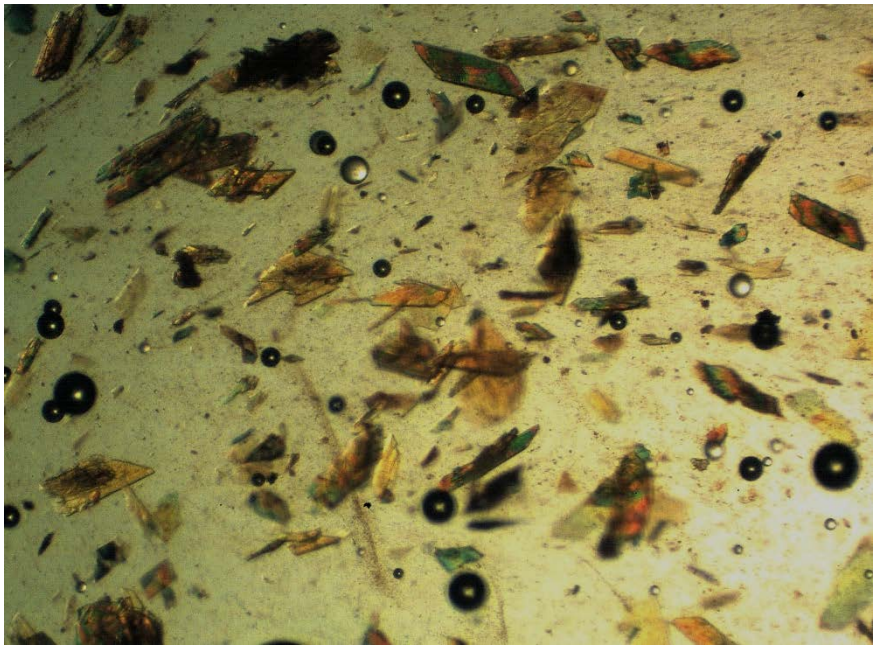

Fig. S9 An optical image of crystals of the Mn_3L_3 framework following metal exchange with $FeCl_2 \cdot 4H_2O$.

Fig. S10 An optical image of crystals of the Mn_3L_3 framework following metal exchange with $FeCl_3$.

Single crystal X-ray structure determinations on Fe-exchanged Mn_3L_3 samples

Full spheres of diffraction data were collected for single crystals mounted on nylon loops in Paratone-N at 100 K on the MX1 beamline of the Australia Synchrotron, λ = 0.71073 Å.[1] N_{tot} reflections were merged to N unique (R_{int} quoted) after 'empirical'/multiscan absorption correction (proprietary software) and used in the full matrix least squares refinements on F^2, N_o with $F > 4\sigma(F)$ being considered 'observed'. Anisotropic displacement parameter forms were refined for the non-hydrogen atoms; hydrogen atoms were treated with a riding model [weights: $(\sigma^2(F_o)^2 + (aP)^2 + (bP))^{-1}$; $P = (F_o^2 + 2F_c^2)/3$]. Neutral atom complex scattering factors were used; computation used the *SHELXL2013* program.[2] Pertinent results are given in the manuscript and in Table S1. CIF data have been deposited with the Cambridge Crystallographic Data Centre, CCDC reference numbers 1443923 ($[Fe_3(L_3)]$-$FeCl_3$) and 1443924 ($[Mn_{3-x}Fe_x(L_3)]$-$FeCl_2$, x = 0.55).

Variata. In the crystal structure of $[Fe_3(L_3)]\cdot FeCl_3$ the metal node of the MOF was refined with an Fe_3 composition (with no allowance made in the refinement for the residual amount of Mn potentially remaining in the node). The MOF structure itself is well behaved with only limited disorder; the commonly encountered disorder of one of the phenyl rings of one of the ligand molecules (not the ligand that is metalated post-synthetically) in the asymmetric unit was refined with two major orientations (0.65:0.35 ratio). The post-synthetically added metal centre is not clearly resolved in this structure as F_{obs} maps reveal (see Figure S11). The metal site itself shows a region of diffuse electron density bounded by two additional regions of electron density in the 'axial' positions of a possible octahedral metal complex and a third region of electron density not on the mirror plane. As noted, we have modelled the electron density as an

octahedral Fe^{3+} cation (due to slightly shorter Fe-N bonds of 2.084(8) Å) possessing two inner-sphere chloride ions and a third outer-sphere anion within the pores of the framework (see Fig. S11 below) but the disorder present limits ultimate confirmation and complete refinement. Residual electron density is located adjacent Fe(3) and Cl(1) with an unreasonably long Fe-Cl distance as a consequence of the apparent disorder. Two moderate peaks in the electron density different map located in the positons normally reserved for non-coordinated anions were refined as sites for the outer-sphere chloride ion with 0.2 occupancy each (both on a mirror plane); no additional positions were identified for the remaining 0.1 occupancy chloride to achieve charge balance.

In the refinement of $[Mn_{3-x}Fe_x(L_3)]$-0.4$FeCl_2$ (x = 0.55) the Fe occupancy of the metalation site was established by trial refinement and determined to be 0.2 (40% occupancy). Using this data and the Fe:Mn ratio for the material, established from inductively-coupled plasma mass spectrometry (ICP-MS), the composition of the metal node was set as $Mn_{2.45}Fe_{0.55}$ and refined with fixed occupancy. Due to the metal occupancy of the bis-pyrazole metalation site only being 40%, meaning that 60% of the ligand does not have a metal centre, there is considerable disorder of the ligand. In other structures of this MOF (without metalation but in DMF and CH_3CN)[3] we see distinct conformations for the non-coordinated ligand . Thus, for this structure, the low occupancy of the metal results in disorder for the bis-pyrazole binding site and the surrounding phenyl ring but the data was not of sufficient quality to allow this disorder to be modelled. Disorder of one of the phenyl rings of the other ligand molecule in the asymmetric unit was refined with two major orientations (0.77:0.23 ratio). The pores of the MOF contain a number of isolated peaks that could not be modelled as solvent

(ethanol due to sample preparation). A peak, assigned as a chloride (0.2 occupancy, 40%) to provide charge balance to added octahedral Fe centre, sits in the pocket typically occupied by anions within the MOF structure.[3] There is additional electron density in this 'anion binding' site (largest peak = 2.958 eÅ^3 before application of the SQUEEZE routine of Platon) but that data is not of sufficient quality for us to build a reasonable structural model for refinement. The SQUEEZE routine of Platon[4] was applied to the data to account for this residual electron density bringing about significant improvements in R_1, wR_2 and GOF.

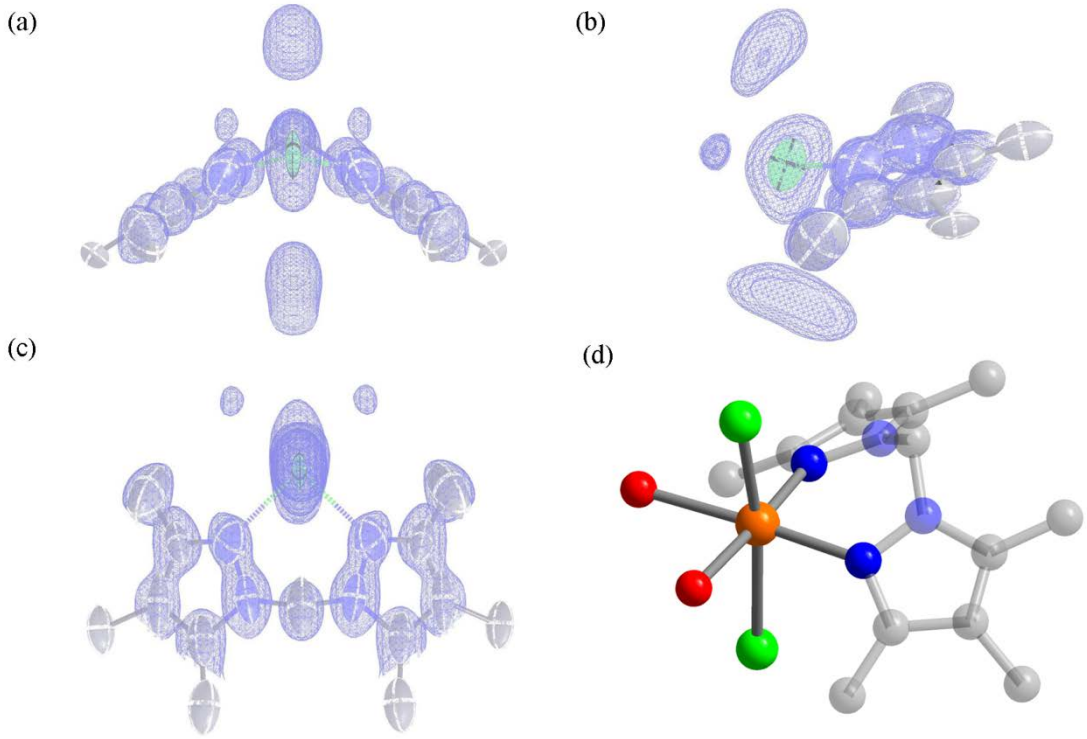

Figure S11. F_{obs} electron density maps showing the electron density in the vicinity of the post-synthetic metalation site in (a) front, (b) side and (c) top views, and (d) an image showing a perspective view of the major occupancy site. The coordination of the Fe consists of two inner-sphere chloride ions, with an outer sphere chloride ion (not shown) for charge compensation. Orange, green, grey, blue, and red spheres represent Fe, Cl, C, N, and O, respectively. H atoms have been omitted for clarity.

Table S1. Crystallographic parameters for the crystal structures of Fe-exchanged Mn_3L_3 samples.

Sample	$Fe_3L_3{\cdot}FeCl_3$	$Mn_{3-x}Fe_x(L_3){\cdot}0.4FeCl_2$ (x=0.55)
Exchange Conditions	$FeCl_3$, acetonitrile, 60 °C, 5 days	$FeCl_2{\cdot}4H_2O$, ethanol, 60 °C, 5 days
Crystallographic Parameter		
Formula	$C_{75}H_{66}Cl_{2.8}Fe_4N_{12}O_{14}$	$C_{75}H_{66}Cl_{0.80}Fe_{0.95}Mn_{2.45}N_{12}O_{13.2}$
FW	1682.05	1562.61
T, K	100(2)	100(2)
Wavelength, Å	0.71073	0.71073
Crystal system, space group	Monoclinic, $P2_1/m$	Monoclinic, $P2_1/m$
Z	2	2
a, Å	12.398 (3)	12.345 (3)
b, Å	33.496 (7)	33.257 (7)
c, Å	12.868 (3)	12.934 (3)
β, °	96.64 (3)	96.66 (3)
V, $Å^3$	5308.0 (19)	5274.4 (19)
d_{calc}, g/cm^3	1.052	0.984
Absorption coefficient, mm^{-1}	0.658	0.486
F(000)	1727	1610
Crystal size, mm^3	0.20 × 0.10 × 0.05	0.30 × 0.10 × 0.05
Theta range for data collection	1.22 - 27.0	1.66 – 27.0
Index range	$-14 \le h \le 14, -40 \le k \le 40, -15 \le l \le 15$	$-16 \le h \le 16, -43 \le k \le 43, -16 \le l \le 16$
Reflections collected	71745	86249
Independent reflections	9914	11740
Data/restraints/parameters	9914 / 1 / 539	11740 / 0 / 539
GOF on F^2	1.301	1.051
Largest diff. peak and hole, $e{\cdot}Å^{-3}$	3.02 and -0.81	1.54 and -1.07
R_1, [I>2σ(I)]	0.1077	0.1036
$R_1(wR_2)$[a], all data	0.1288 (0.3279)	0.1147 (0.2994)
CCDC Number	1443923	1443924

[a] $R_1 = \Sigma||F_o|-|F_c||/\ \Sigma|F_o|$, $wR_2 = \{\Sigma[w(F_o^2-F_c^2)^2]/\ \Sigma[w(F_o^2)^2]\}^{1/2}$

References

[1] T. M. McPhillips, S. E. McPhlllips, H. J. Chiu, A. E. Cohen, A. M. Deacon, P. J. Ellis, E. Garman, A. Gonzalez, N. K. Sauter, R. P. Phizackerley, S. M. Soltis and P. Kuhn, *J. Synchrotron Rad.*, 2002, **9**, 401.

[2] G.M. Sheldrick, Univ. Gottingen, Gottingen, Germany, 2013; *Acta Crystallogr.*, 2008, **A64**, 112; *Acta Crystallogr*. 2015, **C71**, 3.

[3] (a) W. M. Bloch, A. Burgun, C. J. Coghlan, R. Lee, M. L. Coote, C. J. Doonan and C. J. Sumby, *Nat. Chem.*, 2014, **6**, 906. (b) W. M. Bloch, A. Burgun, C. J. Doonan and C. J. Sumby, *Chem. Commun.*, 2015, **51**, 5486.

[4] (a) A.L. Spek, *Acta Crystallogr*., 2009, **D65**, 148; (b) A.L. Spek, *Acta Crystallogr.* 2009, **C71**, 9.